ANNUAL REVIEWS

Annual Review of Materials Research

Microwave Microscopy and Its Applications

Zhaodong Chu, Lu Zheng, and Keji Lai

Department of Physics, University of Texas at Austin, Austin, Texas 78712, USA; email: kejilai@physics.utexas.edu

Annu. Rev. Mater. Res. 2020. 50:1.1–1.26

The *Annual Review of Materials Research* is online at matsci.annualreviews.org

https://doi.org/10.1146/annurev-matsci-081519-011844

Keywords

microwave microscopy, 2D semiconductors, quantum materials, topological edge states, domain walls, microwave acoustics

Abstract

Understanding the nanoscale electrodynamic properties of a material at microwave frequencies is of great interest for materials science, condensed matter physics, device engineering, and biology. With specialized probes, sensitive detection electronics, and improved scanning platforms, microwave microscopy has become an important tool for cutting-edge materials research in the past decade. In this article, we review the basic components and data interpretation of microwave imaging and its broad range of applications. In addition to the general-purpose mapping of permittivity and conductivity, microwave microscopy is now exploited to perform quantitative measurements on semiconductor devices, photosensitive materials, ferroelectric domains and domain walls, and acoustic-wave systems. Implementation of the technique in low-temperature and high-magnetic-field chambers has also led to major discoveries in quantum materials with strong correlation and topological order. We conclude the review with an outlook of the ultimate resolution, operation frequency, and future industrial and academic applications of near-field microwave microscopy.

1. INTRODUCTION

The nanoscale electrodynamic response of solid-state materials is of fundamental importance for research on novel electronic devices with nanometer-sized features, ferroic crystals with mesoscopic domains and domain walls (DWs), strongly correlated materials with spatially inhomogeneous phases, and topological systems with distinct edge and bulk properties. In the far-field regime, however, the result of a measurement is always averaged over a length scale defined by the electromagnetic (EM) wavelength (1). Going beyond this diffraction limit would demand the use of a sharp near-field probe in close proximity with the specimen, usually implemented on a scanning probe microscopy (SPM) platform. In the infrared and visible range of the EM spectrum, such near-field scanning optical microscopy (NSOM) has greatly expanded our knowledge on the mesoscale optical properties of functional materials (2–4). In recent years, the analog of NSOM in the microwave regime, or near-field scanning microwave microscopy (NSMM), has also gained tremendous momentum (4–7). In most cases, the interaction between microwave radiation and materials is much more classical than the optical counterpart. The relative simplicity in the design of NSMM and straightforward data interpretation have led to new types of spatially resolved experiments that are otherwise not feasible.

NSMM was first envisioned in 1928 (8), followed by a few early prototypes (9–12). With the invention of modern SPM, most notably scanning tunneling microscopy (STM) (13) and atomic force microscopy (AFM) (14), various designs of NSMM were demonstrated in the 1990s (15–20). and the focus was mainly on the understanding of the contrast mechanism, the modeling of tip-sample interaction, and the system calibration using standard dielectrics and semiconductors. Excellent reviews of these efforts can be found in References 4–6. In the past decade, much progress was made to integrate microwave probes with state-of-the-art scanning platforms (21–26) and low-temperature/high-magnetic-field chambers (27). Propelled by the rise of quantum materials that are inherently heterogeneous, NSMM has evolved into an important SPM mode for cutting-edge scientific research. While the technique continues to develop and new applications continue to emerge, it is now appropriate to provide a work-in-progress review on the general principle of microwave microscopy, its deployment in materials research, and future prospects for the years to come. We would like to point out that this article is by no means a comprehensive summary of the vast literature in this field, for which the readers are referred to other reviews (4–6). It is rather a survey of the key works and a call for collective efforts to advance this burgeoning area of research.

The rest of this review is organized as follows. In Section 2, we begin by reviewing the basics of microwave microscopy, followed by a description of the system design and data analysis. We then elaborate its applications, categorized by the different material properties probed by the technique, in Section 3. For each subsection, we also discuss the specific targets in the near term. We conclude the review in Section 4 with a summary of the current status and an outlook of this area for the next few decades.

2. NEAR-FIELD MICROWAVE MICROSCOPY

2.1. Basic Principles

Microwaves are commonly defined as the EM radiation with free-space wavelength λ ranging from 1 m (frequency $f = 300$ MHz) to 1 mm ($f = 300$ GHz), although we focus on a narrower band from 300 MHz to 20 GHz here. The interaction between matter and the EM wave in this regime is well understood and widely exploited in day-to-day technology—to name a few, food

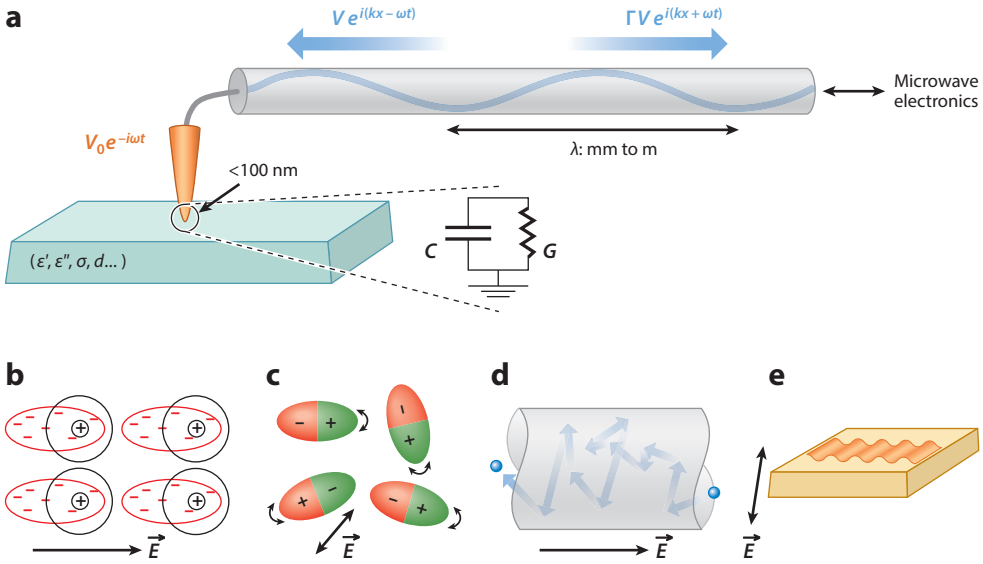

Figure 1

Schematics of microwave impedance microscopy and its contrast mechanism. (*a*) Conceptual sketch of the microwave microscope, showing the excitation and reflection waves in the transmission line, the quasi-static voltage at the nanoscale tip, and the material properties to be probed. The lumped elements representing the tip-sample interaction are shown in the inset. (*b–e*) Illustrations of (*b*) the dielectric response of an insulator to an *E*-field, (*c*) dipolar oscillation in the microwave field, (*d*) diffusive conduction of an electron, and (*e*) excitation of acoustic waves in a piezoelectric crystal by an alternating *E*-field.

is heated in a microwave oven while a microwaveable plate remains lukewarm; an airplane made of metal, on the other hand, reflects microwaves and appears on the radar screen. While sharing the same characteristics, NSMM differs from these phenomena in various aspects. First, while the electric and magnetic parts of the EM energy density are comparable in propagating waves, only one is dominant in each NSMM design (6). In **Figure 1*a***, it is the gigahertz electric field (*E*-field) that is maximized at the electrically open tip. Furthermore, as the typical tip size is approximately six orders of magnitude smaller than the wavelength, the tip-sample interaction can be accurately described by the lumped elements in **Figure 1*a***. Such electrical-impedance-type NSMM is referred to hereafter as microwave impedance microscopy (MIM) (7, 28). Finally, the quasi-static fields only extend into the sample with a dimension determined by the tip apex. To form a near-field image, therefore, one must raster scan the tip on the sample surface.

Illustrations of various MIM contrast mechanisms are shown in **Figure 1*b–e***. The electrical response of a material can be expressed as $\varepsilon' + i(\varepsilon'' + \sigma/\omega)$, where ε' and ε'' are real and imaginary parts of the permittivity, σ is the conductivity, and $\omega = 2\pi f$ is the angular frequency. As depicted in **Figure 1*b***, the response of a perfect insulator to gigahertz *E*-fields is purely capacitive since the displacement current is 90° out of phase with respect to the tip voltage. For materials with permanent dipoles or gigahertz collective modes, the interaction with an oscillating *E*-field leads to dielectric loss (**Figure 1*c***). For electrical conductors, the motion of conduction electrons (**Figure 1*d***) will also result in energy dissipation. Finally, in piezoelectric samples, the electromechanical transduction into gigahertz acoustic waves leads to another channel of energy loss (**Figure 1*e***). Other less common configurations of microwave microscopy are briefly discussed in Section 3.5.

2.2. System Components

The schematic in **Figure 1*a*** is, of course, oversimplified for MIM. The actual system would at least consist of the probe, detection electronics, and the scanning platform. Although metalized tips with a nanoscale apex are readily available for conductive atomic force microscopy (C-AFM), they are unsuitable for MIM due to the strong stray-field contribution from the cantilever body. One design to mitigate this problem, as shown in **Figure 2*a***, is to increase the sample-cantilever distance by a tall (∼80 μm) shank of the metal tip (24, 25), which is commercially available from Rocky Mountain Nanotechnology, LLC. Here, the nanometer-sized apex is achieved by the chemical etching of Pt wires. A more elegant solution is the batch fabrication of shielded cantilever probes (29), which are commercially available from PrimeNano Inc. As indicated in **Figure 2*b***, the Au/Ti/W center conductor is sandwiched between SiN_x layers and shielded by metal layers. The sub-100-nm tip apex is obtained by oxidation sharpening of the sacrificial Si pit and the subsequent metal refill. A drawback here is the inevitable wear during the contact-mode scans, which strongly affects the MIM signal level. In this regard, quartz tuning-fork (TF) probes with etched metal tips (**Figure 2*c***) are desirable not only for the preservation of the tip apex but also for their self-sensing capability in a cryogenic environment (30, 31). The lack of shielding is again circumvented by the high-aspect-ratio probe. The distance modulation in a TF-MIM also rejects the background drift and provides absolute sample information (31). The disadvantages of TF probes are the much harder operation compared with cantilevers and the difficulty tracking rough surfaces due to the small oscillation amplitude (usually <10 nm). Both types of probes will continue to be used in MIM research.

Figure 2*d* shows a schematic of a complete MIM system. Since the impedance of an electrically open tip is very different from 50 Ω in typical transmission lines, an impedance-match (*Z*-match) section is required to ensure efficient power transfer to the probe. Examples of *Z*-match include cavity resonators for needle probes (6) and λ/2 or λ/4 transmission-line resonators for cantilever (28) and TF (30) probes. In **Figure 2*d***, the excitation signal is sent to the tip through a directional coupler and the reflected signal is amplified and demodulated by an in-phase-quadrature mixer, similar to the S_{11} measurement in a vector network analyzer (24, 25). The input microwave power is typically $1 \sim 10$°W, and the measurement is mostly noninvasive (7, 28). As long as the load impedance is a small perturbation to the tip impedance, the imaginary microwave impedance microscopy (MIM-Im) and real microwave impedance microscopy (MIM-Re) parts of the output signals are proportional to the effective tip-sample capacitance and conductance (**Figure 1*a***), respectively. A rigorous derivation of the MIM signals can be found in Reference 32. Finally, it is sometimes necessary to modulate the MIM output by a low-*f* (usually kilohertz) signal, such as voltage modulation for semiconductor samples (33) and distance modulation in the TF operation (30, 31). In this case, lock-in amplifiers are needed to produce the MIM_AC outputs, as depicted in **Figure 2*d***.

A brief introduction to MIM data interpretation is provided at the end of this section. While analytical solutions of certain sample geometries can be obtained (34–37), it is now practical to directly compute the quasi-static admittance (inverse impedance) of an arbitrary tip-sample configuration using the finite-element analysis (FEA) method (7, 28). **Figure 2*e*** plots the simulated MIM signals as a function of the sheet conductance σ_{2D} of a two-dimensional (2D) layer buried 30 nm below the surface of a dielectric sample with $\varepsilon_r = 12$. As a generic feature, the MIM-Im signal increases monotonically with respect to σ_{2D}, whereas the MIM-Re signal peaks at an intermediate σ_{2D} that coincides with the inflection point in MIM-Im. It is obvious that there is an optimal window of σ_{2D} determined by the operation frequency and sample parameters. For materials with large conductivity contrast, MIM-Im is advantageous because of the monotonic response.

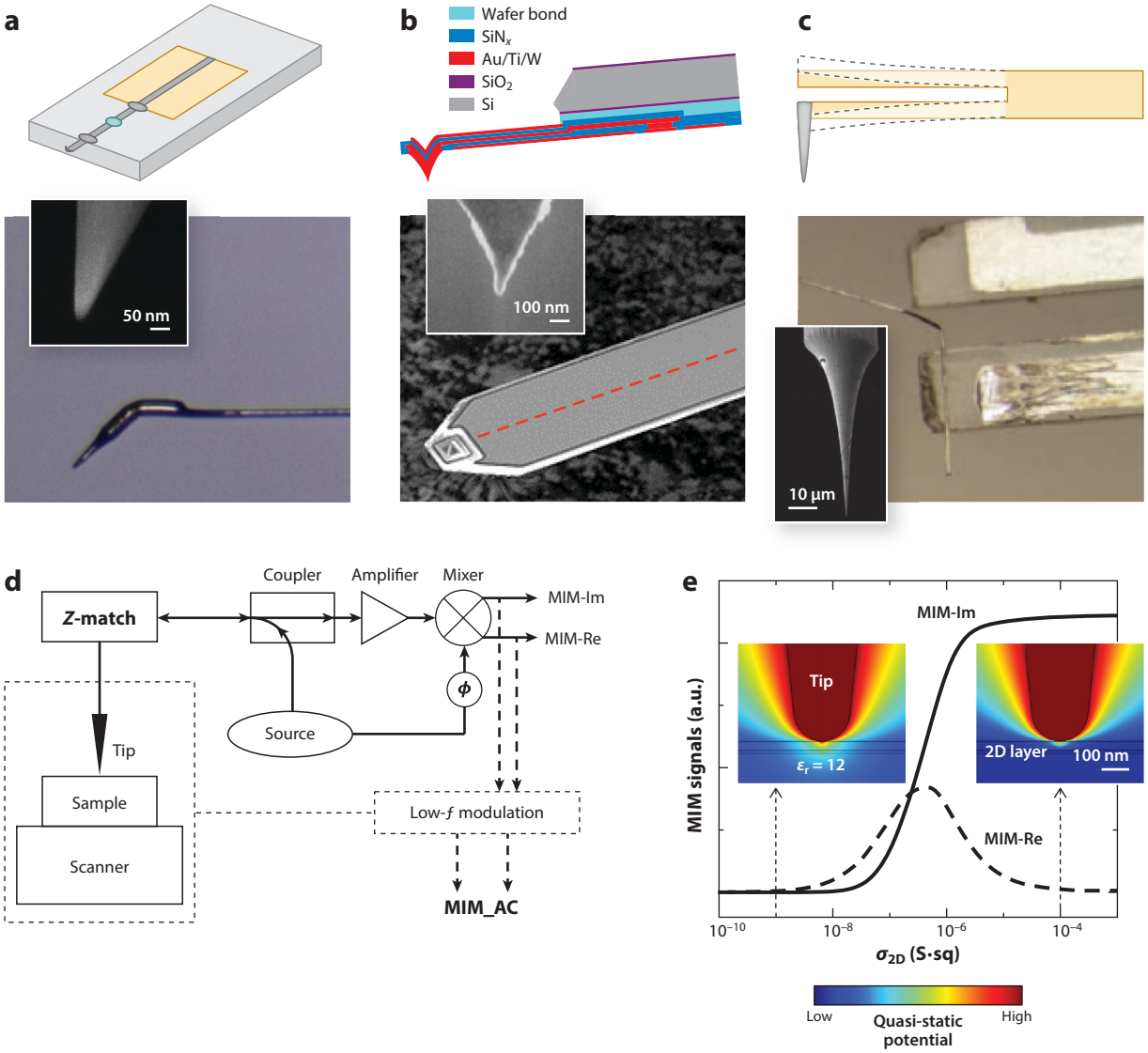

Figure 2

Components of MIM and data interpretation. (*a*, *top*) Schematic of the solid metal probe with a contact pad. (*a*, *bottom*) The cantilever probe with a tall shank of the metal tip. The inset shows the apex of the etched Pt tip. (*b*, *top*) Layer structure of the shielded cantilever probe. (*Bottom*) SEM of the cantilever and pyramidal tip. The red dashed line indicates the buried center conductor. The inset shows the apex of the Au/Ti/W tip. (*c*, *top*) A tuning-fork-based probe. (*Bottom*) An etched W wire (SEM in the *inset*) glued to a tuning fork. (*d*) Schematics of the MIM setup. (*e*) Simulated MIM signals as a function of the sheet conductance of a subsurface 2D layer σ_{2D}. The insets on the left and right show the quasi-static potential distribution maps for $\sigma_{2D} = 10^{-9}$ S·sq and 10^{-4} S·sq, respectively. Abbreviations: MIM, microwave impedance microscopy; MIM-Im, microwave impedance microscopy–imaginary part; MIM-Re, microwave impedance microscopy–real part; MIM_AC, microwave impedance microscopy–alternating current; SEM, scanning electron micrograph. Panel *b* adapted with permission from Reference 29; copyright 2012 IOP Publishing. Panel *c* adapted with permission from Reference 30; copyright 2016 AIP Publishing.

Near the insulating or conductive limits, however, MIM-Re is usually chosen due to the larger d(MIM-Re)/$d\sigma$ here and the small topographic cross-talk. This simple exercise also demonstrates that one cannot directly associate the real and imaginary parts of the dielectric function with the MIM-Re and MIM-Im signals, respectively. Finally, the quasi-static potential at the two limits of σ_{2D} is shown in the inset of **Figure 2*d***. The spatial extent of the E-field (gradient of potential), which defines the spatial resolution of MIM, is comparable to the tip diameter.

3. APPLICATIONS OF MICROWAVE MICROSCOPY

NSMM has many applications in condensed matter physics, materials science and engineering, electrical engineering, and biology, as well as other interdisciplinary research. In the following sections, we group the applications in terms of the contrast mechanism enumerated in **Figure 1**, followed by brief discussions under each category.

3.1. Imaging Dielectric Constant

In an electrical insulator, the ratio between the external E-field and the net field in the medium is defined as its dielectric constant or relative permittivity ε_r. For advanced nanomaterials, the conventional measurement of ε_r involves complicated device fabrication into the parallel-plate geometry. On the other hand, MIM provides a noninvasive method to characterize this fundamental property in the nanoscale.

Figure 3*a* shows the AFM and MIM ($f = 1$ GHz) images of the layered semiconducting chalcogenide In_2Se_3 (38), an important system for phase-change memory, thermoelectric, and photoelectric applications (39). The MIM-Im image exhibits distinct contrast over the mica substrate as a function of the flake thickness, i.e., the signal is lower than mica for a layer number (n) of 3 and higher for $n > 4$. FEA simulation of the MIM data in **Figure 3*b*** shows that the effective ε_r increases monotonically from two to six layers and saturates to the bulk value after $n = 8$, consistent with first-principles calculations (38). The n-dependent ε_r is ubiquitous for van der Waals materials (40), and the methodology is valuable for this vibrant research field.

The gigahertz permittivity of biological systems is also of interest for medical applications as it determines the transmission, reflection, and absorption of microwaves in tissues (41). **Figure 3*c*** shows a schematic of microwave imaging on a single bacterial cell at 19 GHz (42). For the irregular cell structure, the morphologic contribution to the MIM-Im data cannot be ignored. As a result, it is crucial to perform careful calibration to remove the topographic cross-talk from the raw data (**Figure 3*d***). The intrinsic capacitance after subtracting the background is plotted in **Figure 3*d***, showing $\varepsilon_r \sim 4$ with no significant dielectric loss (42). The findings open an important avenue in label-free imaging of single cells with nanoscale spatial resolution.

The two examples reviewed here highlight the potential of MIM as a versatile permittivity imaging tool. Using standard dielectrics as calibration samples (24, 31, 43, 44), this method can be further applied to quantify ε_r of nanoparticles, free-standing films, and granular ceramics, whose nanoscale dielectric response is otherwise difficult to probe.

3.2. Imaging Electrical Conductivity

The imaging of local conductivity is arguably the most successful application of microwave microscopy. In particular, the ability to visualize subsurface conduction is of great interest across many research disciplines. In this section, we first introduce several examples of general-purpose conductivity imaging and then proceed with studies in more specialized areas.

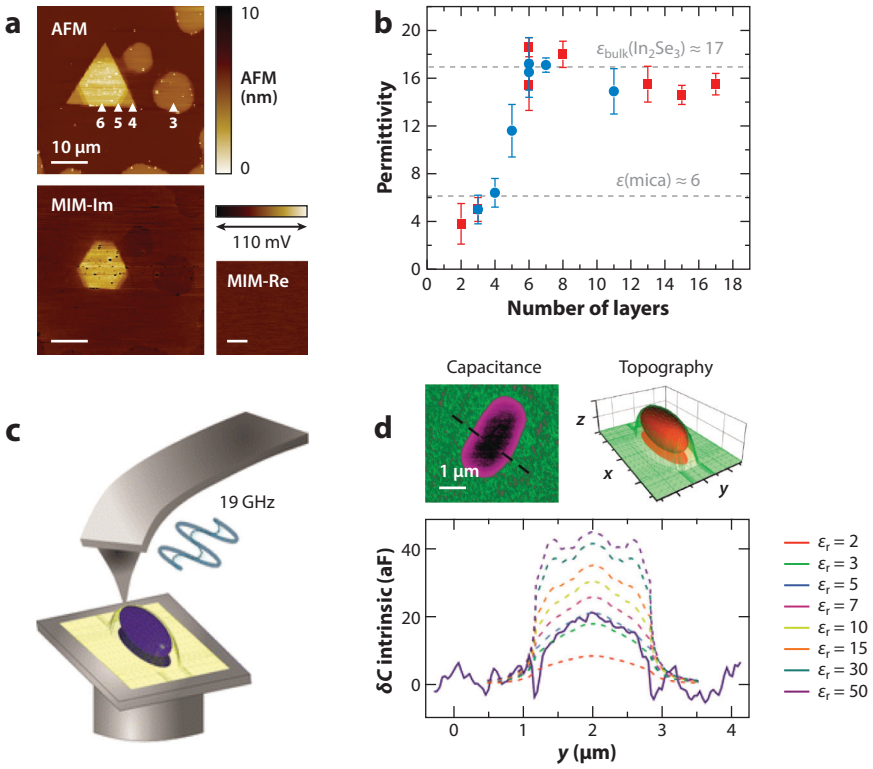

Figure 3

MIM imaging of a dielectric constant. (*a*) AFM (*top*), MIM-Im (*bottom left*), and MIM-Re (*bottom right*) images of few-layer In_2Se_3 nanoflakes. The number of layers *n* is indicated in the AFM image. (*b*) Permittivity deduced from the MIM-Im data as a function of *n*. The blue circles and red squares represent two different batches of samples. (*c*) Schematic of microwave microscopy on a single bacterial cell. (*d*, *top left*) Capacitance image extracted from MIM-Im data. (*Top right*) 3D rendering of the topographic image. (*Bottom*) Comparison of numerically calculated intrinsic capacitance profiles for different dielectric constants (*dashed lines*) of the cell with the experimental intrinsic capacitance profile (*solid line*) after removing topographic cross-talk. The best agreement is found for ε_r ~3–5. Abbreviations: AFM, atomic force microscopy; MIM, microwave impedance microscopy; MIM-Im, microwave impedance microscopy–imaginary part; MIM-Re, microwave impedance microscopy–real part. Panels *a* and *b* adapted with permission from Reference 38; copyright 2015 American Chemical Society (ACS). Panels *c* and *d* adapted with permission from Reference 42; copyright 2016 ACS.

3.2.1. General-purpose studies. With STM-assisted hydrogen resist lithography (45), it is now possible to pattern atomically thin P dopant nanostructures buried in Si wafers, as illustrated in **Figure 4*a***. Characterization of these buried features is important for next-generation information processing, while at the same time presenting a major challenge to SPM tools that do not see through the surface. Using the MIM at $f = 20$ GHz, Gramse et al. (46) were able to image a δ-doped P layer encapsulated with 15-nm Si. In **Figure 4*b***, the nanostructure incorporating P atoms is clearly seen in the capacitance image, whereas the control pattern with the hydrogen desorbed triangle on the right shows no measurable contrast. Note that the conductance channel displays little contrast for both the conductive P-region and the insulating H-region, consistent with the modeling in **Figure 2*e***. The authors reported a lateral resolution of ~40 nm and vertical

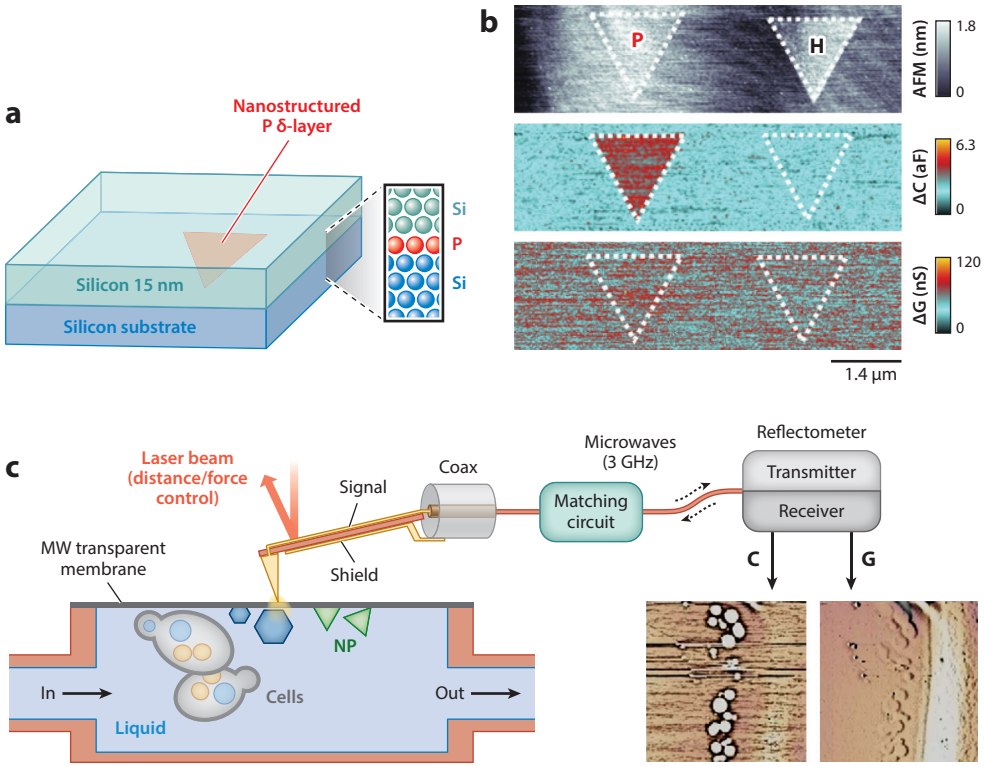

Figure 4

Examples of general-purpose conductivity imaging. (*a*) Schematic of the phosphorus δ-doped layer buried in the Si substrate. (*b*, *top to bottom*) AFM image of a patterned phosphorus and depassivated hydrogen layer and corresponding capacitance (from MIM-Im) and conductance (from MIM-Re) images. (*c*) Schematic layout of the experimental setup. The objects under study are enclosed in a capsule filled with a fluid (or gas) and separated from the probe by an ultrathin dielectric membrane transparent for MW radiation. Abbreviations: AFM, atomic force microscopy; MIM-Im, microwave impedance microscopy–imaginary part; MIM-Re, microwave impedance microscopy–real part; MW, microwave; NP, nanoparticle. Panels *a* and *b* adapted from Reference 46 (CC BY 4.0). Panels *c* and *d* adapted with permission from Reference 47; copyright 2016 American Chemical Society.

resolution of ∼4 nm, suggesting that the technique could aid the development of fabrication processes for surface-code quantum computers (46).

Figure 4*c* demonstrates the MIM imaging of objects in environmental cells (47). Here, the cells and metallic and insulating nanoparticles are enclosed in a capsule filled with a fluid and separated from the probe by an ultrathin dielectric membrane. The same configuration was also utilized to visualize the growth and stripping of Ag dendrites in liquid electrolytes, as well as live yeast cells immersed in glycerol beneath the SiO_2 membrane (47). Since microwave imaging is free from radiolysis and radiation-induced damage, the approach can serve as an ideal framework for in situ studies of fragile organisms and research in reactive, toxic, or radioactive media. The technique can also be coupled with microfluidic platforms for electrophoretic and osmotic controls. The ease of operation and the compatibility with AFM platforms will continue to increase the popularity of MIM in various branches of materials research.

3.2.2. Semiconductors. Semiconductor devices, in which the electrical conductivity is controlled by doping, gating, temperature, or illumination, are the backbone of modern information technology. For the same reason, doped Si and GaAs devices have been the preferred samples for NSMM calibration (25, 28, 33, 48–50). Rather than dwelling on the traditional materials, however, we direct our attention to novel 2D and 1D semiconductors in this review.

Semiconducting transition metal dichalcogenides, such as MoS_2 and WSe_2, are in the limelight of current materials research (51). These layered materials can be exfoliated into atomically thin 2D sheets with unique electrical and optical properties, which are attractive for nanoelectronics and optoelectronics. **Figure 5*a*** shows the transfer curve of a few-layer MoS_2 flake in the field-effect transistor (FET) configuration (52). The device was covered by 15-nm-thick Al_2O_3 to avoid direct contact between the metallic tip and the 2D sheet. **Figure 5*b*** displays selected MIM images within the channel region as a function of the back-gate voltage (V_{BG}). As V_{BG} increased, the conductance signal emerged initially at the edges and then in the interior, with appreciable spatial nonuniformity (52). For quantitative analysis, average MIM-Im/Re signals on the four- and three-monolayer segments in **Figure 5*b*** are plotted in **Figure 5*c***, which are consistent with the simulated response curves (**Figure 2*e***). The results suggest that the contribution of defect-induced edge states to the total conductance is significant in the subthreshold regime but negligible once the bulk becomes conductive. The observation of conductance inhomogeneity also provides a guideline for future improvement of the device performance. Similar MIM works have been carried out on other 2D materials (53–62).

It is a common practice of MIM to modulate the local carrier concentration by applying a low-f (kilohertz) voltage (V_{AC}) on the tip (**Figure 5*d***). The demodulated signal is recorded to form MIM_AC or microwave impedance modulation microscopy (MIM^2) images during the scan (63). The configuration is similar to that in scanning capacitance microscopy, where the n- and p-doped regions exhibit opposite dC/dV signals (64). The combined MIM and MIM^2 allows more detailed analysis of the sample. **Figure 5*e*** shows the MIM, MIM^2, and AFM data on an array of carbon nanotubes (CNTs) (63). For metallic CNTs, the large amount of carriers led to strong MIM and negligible dC/dV signals. At low V_{AC}, semiconducting CNTs displayed appreciable MIM^2 signals, with p-doped tubes showing unipolar $+\Delta C$ and intrinsic tubes showing bipolar $\pm\Delta C$ on the two polarities of V_{AC}. Finally, for semimetallic CNTs, strong MIM^2 signals appeared at high V_{AC}. The MIM tip modulation was also applied to other nanowire systems (65–67).

Using the FET configuration, either tip bias or sample bias, the Fermi level of the semiconducting materials can be locally modulated. The MIM/MIM^2 is thus similar to the STM/scanning tunneling spectroscopy measurement, with lower resolution but much relaxed requirements for sample preparation and environment control. MIM also would be useful for novel semiconductor devices, such as ferroelectric FETs (68) and electric double-layer transistors (69), which was demonstrated recently (70, 71).

3.2.3. Photoconductors. Photoconductivity, the drastically altered electrical conductivity in a material under optical illumination, is widely exploited in optoelectronics. With some exceptions for semimetals and correlated materials, most photoconductors are also semiconductors. Considering the addition of a light source and optical components in the setup, however, light-illuminated microwave impedance microscopy (iMIM) deserves a separate section here. Note that iMIM, which measures the intrinsic photoconductivity without the need of electrodes, is fundamentally different from scanning photocurrent microscopy, which maps out the photo-generated current across the source and drain electrodes when a focused laser beam scans over the device (72).

The worldwide surge of research interest in organic-inorganic trihalide perovskites, e.g., $CH_3NH_3PbI_3$ or $MAPbI_3$, has led to a phenomenal increase in the power conversion efficiency from 3.8 to 24.2% in the past few years (73). **Figure 6*a*** shows a schematic of a recent iMIM study, in which the tip was aligned with a focused laser beam illuminated through a transparent glass substrate (74). When the perovskite solar cell film was in the dark, the MIM signals indicated the absence of mobile carriers. When illuminated by an above-gap laser with $\lambda = 532$ nm, however, clear photoconductivity was seen in the MIM images (**Figure 6*b***). Interestingly, while the MIM-Im image shows appreciable topographic cross-talk, the MIM-Re image is rather uniform across

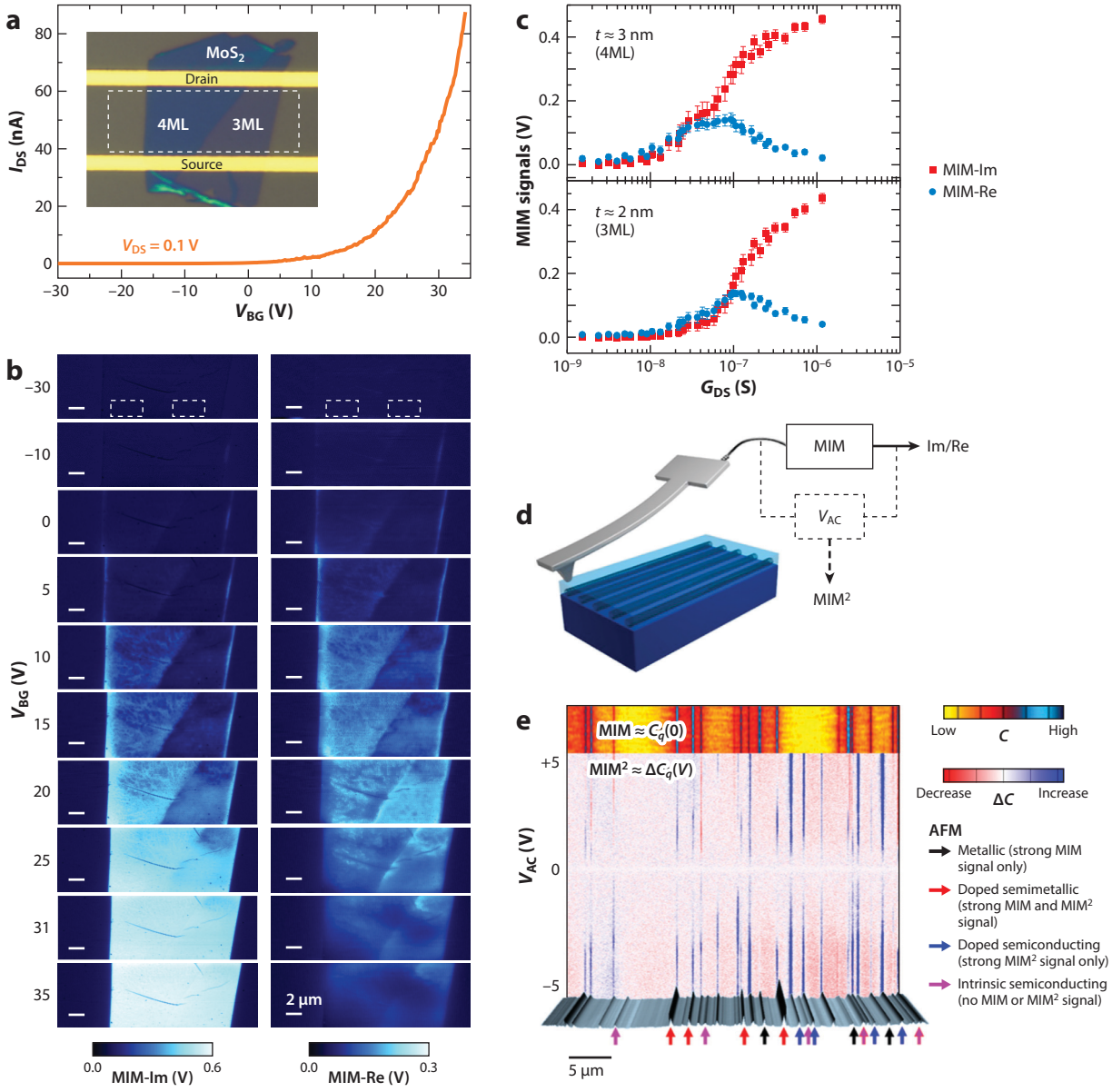

(*Caption appears on following page*)

Figure 5 (*Figure appears on preceding page*)

MIM imaging on semiconductors. (*a*) Transfer characteristics of the back-gated MoS_2 transistor. The inset shows a picture of the device. (*b*) Selected MIM images of the sample in the dashed box in panel *a*. (*c*) Averaged MIM signals as a function of the source-drain conductance for the 4ML and 3ML regions in the dashed boxes in panel *b*. (*d*) Schematic of MIM and MIM^2 experiments on encapsulated carbon nanotubes. (*e*, *top to bottom*) MIM, MIM^2, and AFM topography scans of the same nanotube array, illustrating the complementary nanoscale data obtainable with each technique. The signatures have been categorized for the four electronic nanotube types indicated by the colored arrows: strong MIM signal only (*black*, metallic), strong MIM^2 signal only (*blue*, lightly doped semiconducting), both strong MIM and MIM^2 signals (*red*, semimetallic), and no signal with either technique (*purple*, intrinsic semiconducting). Abbreviations: 3ML, three monolayer; 4ML, four monolayer; AFM, atomic force microscopy; MIM, microwave impedance microscopy; MIM^2, microwave impedance modulation microscopy; MIM-Im, imaginary microwave impedance microscopy; MIM-Re, real microwave impedance microscopy. Panels *a–c* adapted with permission from Reference 52; copyright 2016 Proceedings of the National Academy of Sciences. Panels *d* and *e* adapted with permission from Reference 63; copyright 2016 American Chemical Society.

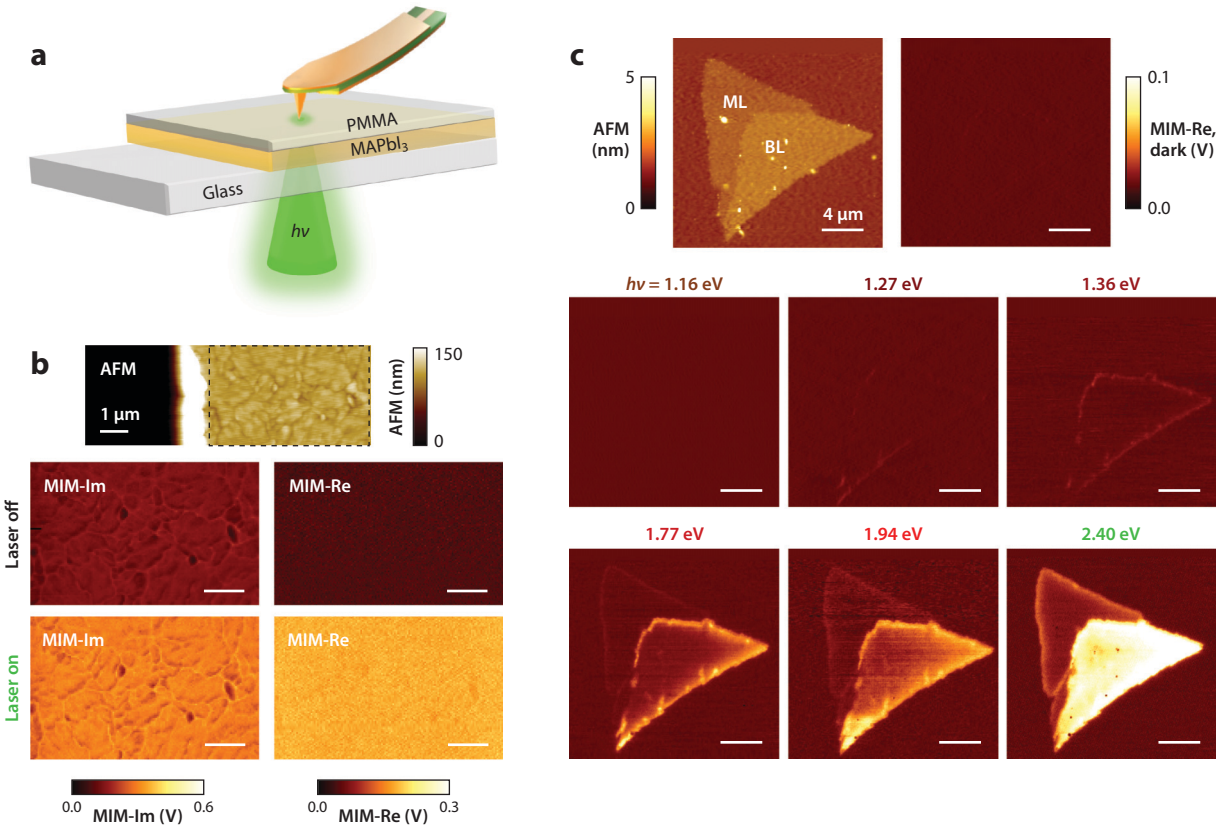

Figure 6

Photoconductivity imaging by iMIM. (*a*) Schematic of the hybrid perovskite sample and the iMIM setup with bottom illumination through the transparent glass substrate. Scanning is accomplished by moving the sample stage while fixing the laser beam and the probe tip, which are aligned before the experiment. (*b*) AFM (*top*) and MIM-Im/Re images (inside the *black dashed rectangles* in the AFM data) when the 532-nm laser is turned off (*middle*) and on (*bottom*). (*c*) AFM and MIM-Re images of an ML-BL WSe_2 flake when illuminated by diode lasers with different energies, showing the sequential emergence of photoconductivity in different regions of the sample. Abbreviations: AFM, atomic force microscopy; BL, bilayer; iMIM, light-illuminated microwave impedance microscopy; MIM-Im, microwave impedance microscopy–imaginary part; MIM-Re, microwave impedance microscopy–real part; ML, monolayer; PMMA, polymethyl methacrylate. Panels *a* and *b* adapted from Reference 74 (CC BY 4.0). Panel *c* adapted with permission from Reference 77; copyright 2018 American Chemical Society.

grains and grain boundaries, suggesting that microstructures do not lead to strong spatial variations of the intrinsic photo-response. The same work also showed that the degradation process began with the disintegration of grains rather than nucleation and propagation from visible grain boundaries (74). Such understanding of the defect structures, grain boundaries, and air stability is important to improve the device performance towards commercialization.

Vertical and lateral heterostructures of 2D materials provide tremendous flexibility to engineer local band structures (75, 76). **Figure 6*c*** shows the MIM images of photoconductivity in a monolayer-bilayer WSe_2 lateral heterostructure under multiple excitation lasers (77). As the photon energy increased from 1.16 to 2.40 eV, the light-induced conductivity first appeared along the hetero-interface and bilayer edge, then along the monolayer edge, inside the bilayer area, and finally in the interior of the monolayer region. The sequential emergence of mobile carriers in different sections of the sample can be used to construct a qualitative configuration of local energy gaps, which is consistent with the density functional theory calculations (77). The results suggest the exciting possibility of band-gap engineering on the length scale of nanometers.

Photoconductivity imaging is still in its infancy (74, 77, 78–80) and will likely see rapid growth in the next few years. First, it is straightforward to use a broadband light source to determine the onset of free-carrier generation. The electronic gap measured by iMIM is different from the optical gap determined from absorption experiments, as the latter is reduced by the exciton binding energy (51). Second, by moving the tip with respect to the laser spot, a diffusion map of the photo-generated carriers can be obtained. Third, by using a pulsed laser and fast electronics, the microwave response can be temporally resolved down to 1–10 ns, which will be a powerful method to study the dynamics of photo-excited electrons. Finally, the measurements can be incorporated in a cryogenic environment to suppress the thermal excitation.

3.2.4. Strongly correlated systems. Strongly correlated materials are a wide class of compounds whose behaviors cannot be described by noninteracting or weakly interacting physics (81). A defining feature of these systems is the emergence of unusual electronic and magnetic properties (82). In particular, the electron correlation may lead to the coexistence of competing states with drastically different electronic structures, whose spatial configurations closely reflect the underlying physics. MIM would be an ideal tool to probe such coexisting domains or domain boundaries.

Figure 7*a* shows the low-T magneto-transport data of the colossal magnetoresistive material $Nd_{0.5}Sr_{0.5}MnO_3$ with coexisting charge/orbital-ordered insulating phase and ferromagnetic metallic (FM-M) phase (83). As the magnetic field increased from 2.4 to 9.0 T, the macroscopic transport resistivity dropped by four orders of magnitude, accompanied by substantial expansion of the FM-M phase in the MIM-Im image (**Figure 7*b***). The FM-M phase at high field formed an interconnected network, with a volume fraction consistent with the 2D percolation transition (inset of **Figure 7*a***). Strikingly, the prominent FM-M filaments aligned preferentially along the [001] and $[1\bar{1}0]$ directions of the substrate, suggesting the anisotropic elastic strain as the key interaction here (83). Metal-insulator transitions in complex oxides such as VO_2 (84, 85) and $Pr_{1-x}(Ca,Sr)_xMnO_3$ (86) were also imaged by MIM.

In a magnetic insulator, whether metallic behavior occurs at the DWs is a long-standing question that remains elusive experimentally (87). **Figure 7*c*** shows a schematic of the low-T insulator $Nd_2Ir_2O_7$ with unusual all-in-all-out (AIAO) magnetic orders (88). The zero-field MIM-Im image of a polished polycrystalline sample is displayed in **Figure 7*d***, showing highly conductive curvilinear features with respect to the insulating bulk (89). In contrast, most conductive curves disappeared under 9 T, which aligned the magnetic domains and eliminated the AIAO DWs. As supporting evidence, the transport conductance across two electrodes fabricated on the sample

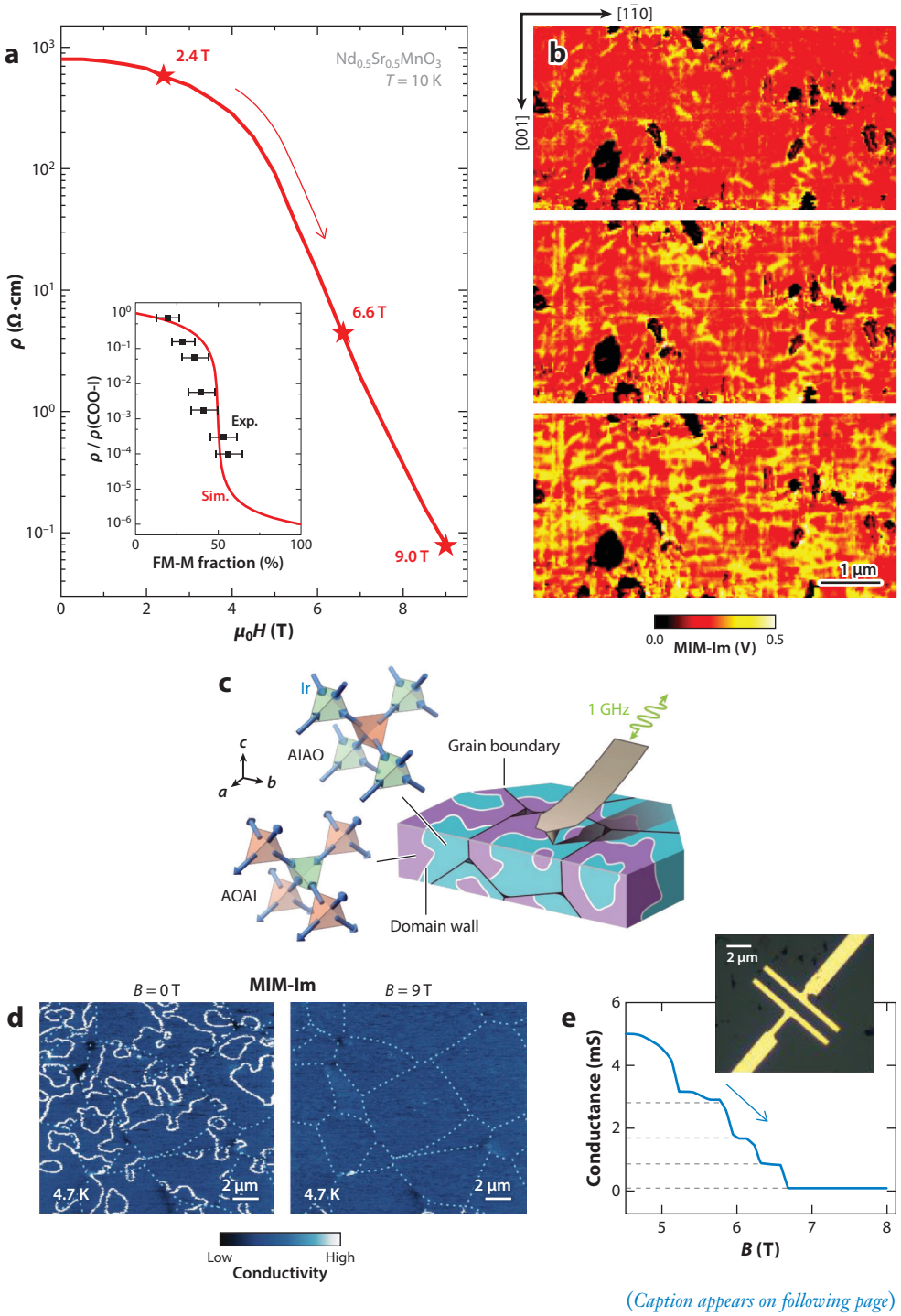

(Caption appears on following page)

Figure 7 (*Figure appears on preceding page*)

MIM application on strongly correlated materials. (*a*) Resistivity of an $Nd_{0.5}Sr_{0.5}MnO_3$ thin film during the field sweep at 10 K. The three fields at which MIM images were taken are marked by red stars. The inset shows a comparison between the 2D square-lattice simulation (*red curve*) and the experimental data (*black squares*). (*b*) MIM-Im images taken at 2.4, 6.6, and 9.0 T. The ferromagnetic metallic phase (*yellow*) exhibits higher signals than the charge/orbital-ordered insulating phase (*red*). The black particles are MnO_x defects. (*c*) Illustration of the MIM scanning setup on polished polycrystal $Nd_2Ir_2O_7$, showing the spin configuration of the AIAO order and its variations. Domain walls can exist between the two variations. (*d*, *left*) MIM-Im image taken after zero-field cooling from 40 to 4.7 K. The dotted lines are grain boundaries, and the dark spots are voids between grains. Curvilinear features much more conductive than the bulk are AIAO magnetic domain walls. (*Right*) MIM-Im image in the same region after a thermal cycle to 40 K and cooling back to 4.7 K in 9 T. Most grains become single domain. (*e*) Typical conductance versus magnetic field of a microelectrode device (*inset*) at 2 K, showing staircase-like drops. Abbreviations: AIAO, all-in-all-out; AOAI, all-out-all-in; exp., experiment; FM-M, ferromagnetic metallic; MIM, microwave impedance microscopy; MIM-Im, microwave impedance microscopy–imaginary part; sim. simulation. Panels *a* and *b* adapted with permission from Reference 83; copyright 2010 American Association for the Advancement of Science (AAAS). Panels *c*–*e* adapted with permission from Reference 89; copyright 2015 AAAS.

showed abrupt drops as the field ramped up (**Figure 7*e***), consistent with the sequential removal of DWs between the electrodes. The results unambiguously establish the metallic nature of DWs in this AIAO magnetic insulator. Enhanced conductivity was also observed in charge-ordered DWs in the layered manganite $Pr(Sr_{0.1}Ca_{0.9})_2Mn_2O_7$ (90).

Local imaging on strongly correlated materials has been very fruitful to date, as exemplified by the study of nanoscale inhomogeneity in unconventional superconductors by STM (91). The highly resistive phases in many complex oxides, however, are difficult to study by a tunneling experiment. Similarly, while NSOM has become increasingly important in the imaging of correlated systems (92), it is mostly sensitive to the optical contrast between metals and insulators. As already demonstrated above, MIM is in a unique position to continue the investigation on these intriguing quantum materials.

3.2.5. Topological quantum systems. The research on the topologically ordered phase of matter (93, 94) has been in the central stage of quantum science and engineering. In particular, the dissipationless edge or surface states may enable novel memory and logic technologies with minimal energy consumption. While these conductive channels have been demonstrated by macroscopic measurements, much remains to be explored on their microscopic details.

The integer quantum Hall effect (IQHE) is characterized by the exact quantization of the Hall resistance and vanishing longitudinal resistance (95). As illustrated in **Figure 8*a***, the topological boundary states are formed by the intersection between Landau levels (LLs) and the Fermi level (E_F) of a high-mobility 2D electron system (2DES) under high magnetic (B) fields. **Figure 8*b*** shows the MIM images at $T = 2.3$ K and $B = 5.4$ T of a GaAs/AlGaAs 2DES etched into isolated disks (96). Immediately inside the physical boundary, the strong MIM-Im and zero MIM-Re signals are indicative of a metallic strip around the perimeter. The MIM imaging also enabled quantitative measurement of the width of edge states, and the result is in good agreement with the electrostatic model (97). A follow-up experiment was performed in a graphene flake, and the IQHE edges were again imaged (98).

Different from the IQHE at high B-fields, the quantum spin Hall effect (QSHE) shows a quantized spin Hall conductance and a vanishing charge Hall conductance at $B = 0$ (99, 100). As illustrated in **Figure 8*c***, the QSHE features a bulk energy gap and a pair of gapless helical edge states carrying opposite spins. **Figure 8*d*** shows MIM line scans across two HgTe/$(Hg_{0.3}Cd_{0.7})$Te quantum well (QW) devices as E_F was tuned by the back gate (101). For the topologically trivial

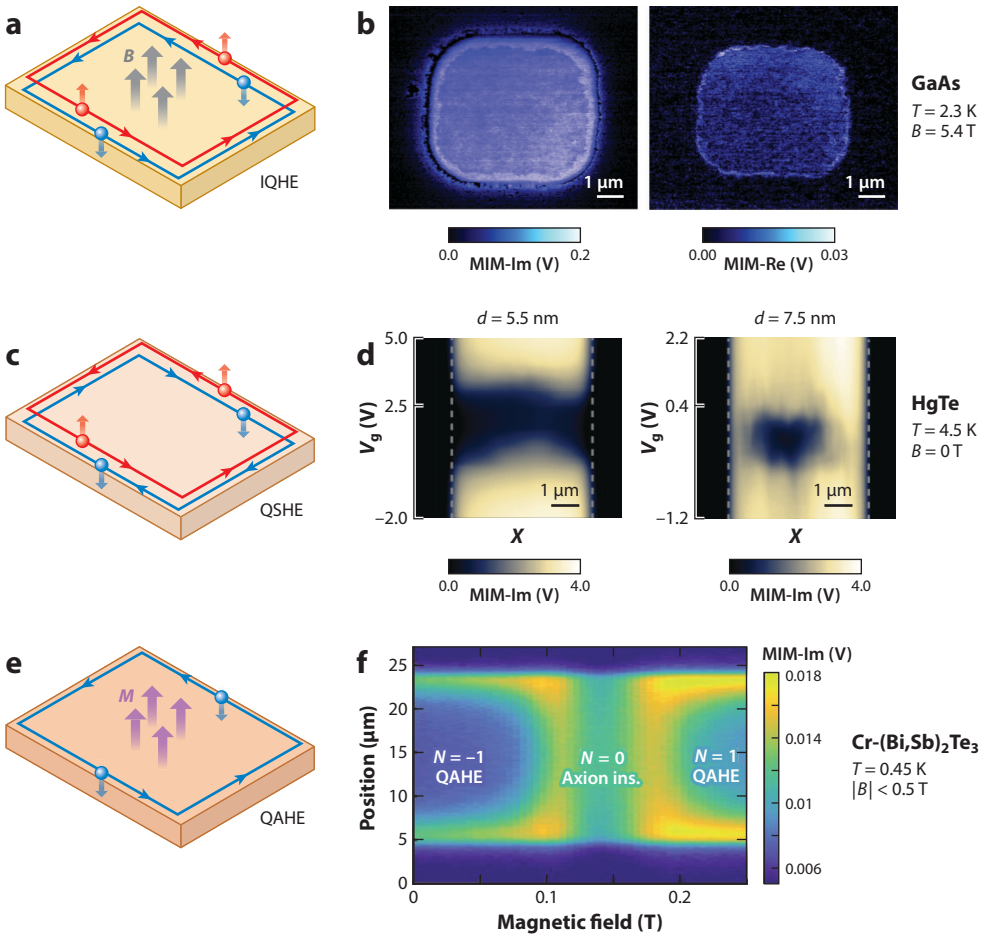

Figure 8

Microwave imaging of topological edge states. (*a*) Schematic of the IQHE under high magnetic fields. (*b*) MIM images at $B = 5.4$ T and $T = 2.3$ K of a high-mobility GaAs 2D electron system. Conductive edge channels are clearly seen around the physical boundary of the etched disk. (*c*) Schematic of the QSHE under zero magnetic field. (*d*) Zero-field MIM single-line scan versus gate voltage across an HgTe/$(Hg_{0.3}Cd_{0.7})$Te device with a quantum-well thickness of 5.5 nm (*left*) and 7.5 nm (*right*). Within the bulk gap region, conductive edges are absent in the topologically trivial sample on the left and present in the QSHE sample on the right. (*e*) Schematic of the QAHE with an out-of-plane magnetization. (*f*) MIM-Im line scan across a Cr-doped $(Bi,Sb)_2Te_3$ sample versus the magnetic field, showing the evolution of edge states across the two QAHE states and the axion insulator state. Abbreviations: axion ins., axion insulator; IQHE, integer quantum Hall effect; MIM, microwave impedance microscopy; MIM-Im, microwave impedance microscopy–imaginary part; MIM-Re, microwave impedance microscopy–real part; QAHE, quantum anomalous Hall effect; QSHE, quantum spin Hall effect. Panel *b* adapted with permission from Reference 96; copyright 2011 American Physical Society. Panel *d* adapted from Reference 101 (CC BY 4.0). Panel *f* adapted with permission from Reference 107; copyright 2019 Proceedings of the National Academy of Sciences.

sample with a QW thickness d of 5.5 nm (below the critical value of 6.5 nm), the entire sample became insulating inside the bulk gap. For the nontrivial sample with $d = 7.5$ nm, however, the bulk turned insulating but the two edges remained conductive as E_F passed through the bulk gap, consistent with the QSHE physics in HgTe (102, 103). The QSHE edge states in monolayer WTe_2 flakes were also visualized by MIM in a recent work (104).

In analogy to the $N = 1$ (N being the LL index or the first Chern number) IQHE state, the quantum anomalous Hall effect (QAHE) is characterized by a chiral 1D edge current that encloses an insulating bulk (105, 106). The time-reversal symmetry, however, is broken by a spontaneous out-of-plane magnetization (**Figure 8*e***) rather than an external B-field. **Figure 8*f*** shows the MIM line scans across a Cr-$(Bi,Sb)_2Te_3$ sample with two magnetically doped layers (107), whose magnetization was controlled by a small B-field (<0.5 T). For the $N = \pm 1$ states, the hallmark of QAHE, i.e., dissipationless edges and insulating bulk, was vividly imaged by the MIM. In between the two QAHE states, however, the system entered a topologically distinct axion insulator ($N = 0$) state (108–110) with spatially uniform conductivity, where the magnetization direction was opposite in the two magnetic layers. The visualization of both QAHE and axion insulator states further testifies to the ability of MIM to probe exotic quantum states.

In the past decade, many topologically nontrivial states have been theoretically proposed and experimentally realized. Given its nanoscale resolution, strong electrical contrast, noninvasive nature, and compatibility with a high-B/low-T environment, MIM may become indispensable for probing topological materials. In the meantime, the interpretation of MIM data in the quantum regime needs to be improved to include ballistic transport (rather than diffusive transport in **Figure 1*d***) for high-mobility samples and topological channels, as well as the full resistivity tensor with a nontrivial Hall contribution. It is likely that what we have seen here is merely the tip of the iceberg, leaving open space for future explorations.

3.3. Imaging Dielectric Loss

The dielectric loss in a material quantifies the dissipation of EM energy due to dipolar relaxation or the excitation of collective modes (111). At a fixed frequency, the dipolar loss $\varepsilon''\omega$ is indistinguishable from the electronic conduction σ at the circuit level. To separate the contributions between mobile carriers and bound charges, therefore, one must perform simultaneously DC (usually by C-AFM) and AC (usually by f-dependent MIM) microscopy for the mapping of local dielectric loss in complex systems.

When a multidomain ferroelectric is placed in microwave fields, the coupling between the spontaneous polarization and the alternating E-field may lead to periodic oscillation of the DWs and, thus, dielectric loss (112–114). On the other hand, it is now widely accepted that many ferroelectric DWs can host electrical conduction due to the presence of free carriers (115, 116). For weakly charged walls in $KNbO_3$ crystals (117) and transiently formed charged walls in lead zirconate titanate thin films (118), the gigahertz DW conductivity measured by MIM is indeed dominated by charge carriers. The situation, however, is different for the neutral walls on hexagonal manganites (h-$RMnO_3$). **Figure 9*a*** shows piezo-force microscopy (PFM), C-AFM, and MIM images on the [001] surface of $YMnO_3$ (119). The C-AFM data showed that the DWs are more resistive than the adjacent domains (120) with a DC conductivity $\sim 10^{-3}$ S/m. On the other hand, the MIM images in the same area indicate very strong gigahertz response at the DWs. For comparison, the DW signals were quantified by an effective gigahertz conductivity, which is as high as ~400 S/m from the FEA. The f-dependent DW conductivity (**Figure 9*b***) was measured by a series of MIM electronics, showing a peak-like feature around 3 GHz. The result established that the DW vibration (inset of **Figure 9*b***), rather than electronic conduction, is responsible for the

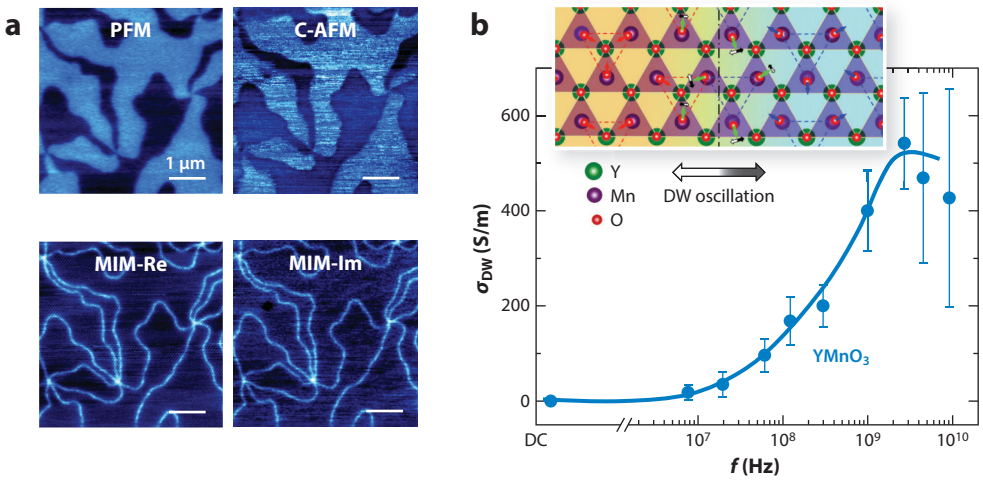

Figure 9

Imaging of dielectric loss by MIM. (*a*) PFM, C-AFM, and MIM images acquired on the [001] surface of $YMnO_3$. The cloverleaf-like domain patterns are seen in the PFM and C-AFM images, whereas the DWs are highlighted in the MIM data. (*b*) Frequency-dependent effective DW conductivity. The blue line is a visual guide. The inset shows an atomistic view of $YMnO_3$ in the [001] plane across the interlocked antiphase boundary and ferroelectric DW. The black and white double-headed arrow illustrates the amplitudes and directions of the periodic DW sliding. Abbreviations: C-AFM, conductive atomic force microscopy; DW, domain wall; MIM, microwave impedance microscopy; MIM-Im, microwave impedance microscopy–imaginary part; MIM-Re, microwave impedance microscopy–real part; PFM, piezo-force microscopy. Figure adapted from Reference 119 (CC BY 4.0).

pronounced dielectric loss (119). Similar behavior was also seen in hexagonal ferrite (h-RFeO$_3$) (121). It should be emphasized that the DW physics in ferroelectric $YMnO_3$ is different from that in the magnetic insulator $Nd_2Ir_2O_7$ (**Figure 7*d***) (89), where the walls are equally conductive at DC and microwave frequencies.

The measurement of an f-dependent dielectric response will undoubtedly lead to follow-up investigations on other ferroelectric DWs. More importantly, broadband MIM will open up enormous opportunities to locally probe materials with gigahertz collective modes, such as charge density waves (122) and pinned Wigner crystals in 2DES (123). Since the dielectric loss in these samples is specific to the microwave frequency, MIM would be the only technique to map out their gigahertz dynamics in the nanoscale.

3.4. Imaging Electroacoustic Transduction

In a piezoelectric material, the mechanical stress is coupled to the electric potential by the linear electromechanical interaction. An oscillating gigahertz E-field, therefore, will launch acoustic waves in the sample. Such electroacoustic transduction has found many applications in electronic components such as surface acoustic wave (SAW) devices (124). For MIM on piezoelectrics, this new channel of energy dissipation, in addition to the usual dielectric response, should be taken into account for image analysis (125, 126).

Figure 10*a* shows the results on a z-cut $LiNbO_3$ sample with one long DW (126). The two oppositely polarized domains are seen in the PFM image. The MIM-Re image, on the other hand, exhibits clear interference fringes around the wall. As the electrical conductance of $LiNbO_3$

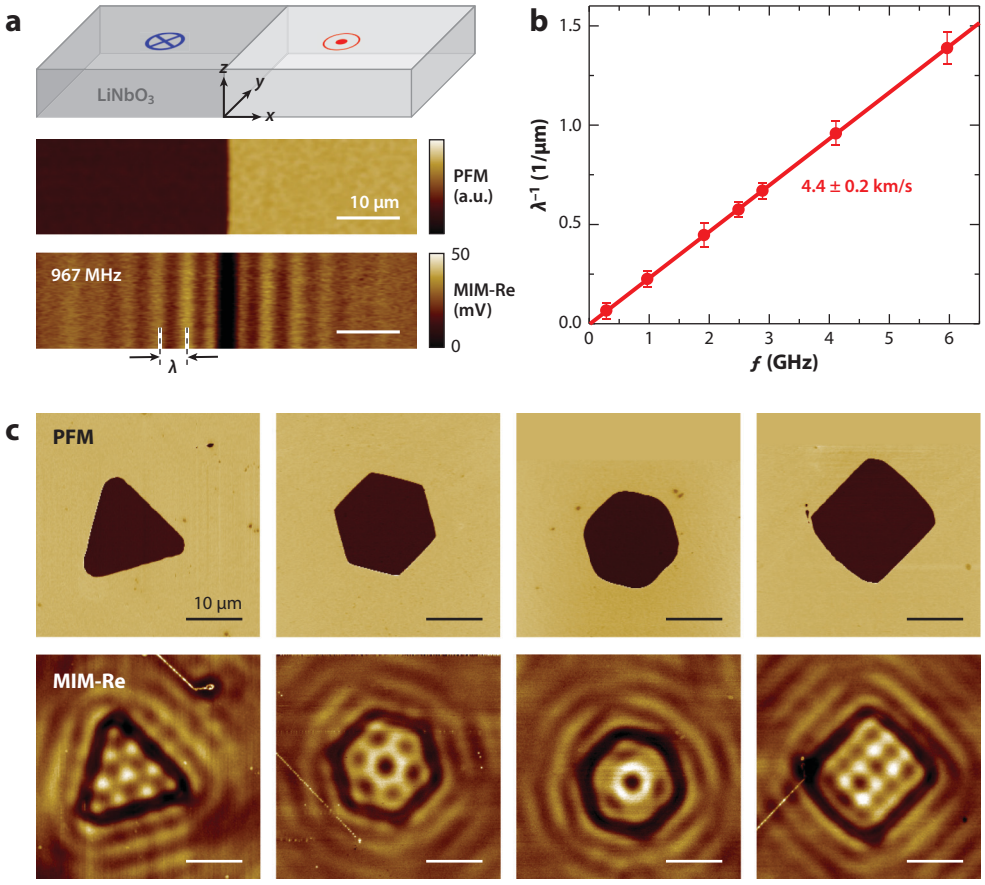

Figure 10

MIM imaging on piezoelectric power transduction. (*a*, *top to bottom*) Schematic, PFM, and MIM-Re images of the *z*-cut $LiNbO_3$ crystal with a single domain wall in the middle. The MIM image exhibits clear interference fringes, with a period of λ labeled in the plot, around the DW. (*b*) Linear relation between 1/λ and the MIM frequency. The slope corresponds to a wave velocity of 4.4 ± 0.2 km/s. (*c*) PFM and MIM-Re images of four $LiNbO_3$ coral domains. Clear interference patterns due to the superposition of ripples around each DW are seen in the MIM-Re data. Abbreviations: DW, domain wall; MIM, microwave impedance microscopy; MIM-Re, microwave impedance microscopy–real part; PFM, piezo-force microscopy. Figure adapted with permission from Reference 126; copyright 2018 Proceedings of the National Academy of Sciences.

is negligible, the MIM-Re contrast indicates that the microwave energy is dissipated through piezoelectric transduction rather than Ohmic loss. In **Figure 10*b***, the measured 1/λ (λ being the period of the MIM-Re fringes) is plotted as a function of the MIM frequency. The slope of 4.4 ± 0.2 km/s closely matches that of the *x*-propagating pseudo-SAW on *z*-cut $LiNbO_3$ (127). Using electrometrical FEA, one can simulate the one-λ oscillation in energy loss as the tip moves away from the DW, which stems from the nonlocal interaction between electric fields and elastic waves (126). The interference of piezoelectric transduction can be further appreciated in $LiNbO_3$ coral domains (126), as seen from **Figure 10*c***.

MIM of ferroelectric domains reveals certain internal degrees of freedom in piezoelectric and elastic tensors, which are not accessible by measurements of the acoustic displacement

fields. Continued work along this line may open a new research frontier to explore nanoscale electroacoustic phenomena in complex structures.

3.5. Beyond Electrical Impedance Imaging

While the majority of NSMM applications to date are the electrical impedance type, exceptions exist for imaging other material properties, which are briefly discussed here.

3.5.1. Imaging magnetic impedance. To probe the microwave magnetic response, one needs to modify the lumped-element model in **Figure 1*a*** to include the tip-sample mutual inductance. The coupling to the electrically open tip described above is relatively weak (128). On the other hand, an electrically short or loop tip that maximizes microwave magnetic fields around the probe head would enable study of the local permeability and magnetic resonance (6). Given the difficulty of forming a nanoscale loop probe and the competing technology in magnetic imaging, the success of this research area is still pending future developments.

3.5.2. Imaging gigahertz nonlinearity. The local higher-order dielectric or magnetic properties can be measured by probing the nanoscale nonlinear response. In practice, one can either apply kilohertz modulation to the gigahertz excitation and demodulate the higher-order signals or directly detect the higher harmonics of the gigahertz signals. By using the former scheme, scanning nonlinear dielectric microscopy has achieved appreciable success in ferroelectrics (129) and semiconductors (130). Similarly, by using a loop probe and the latter scheme, investigators have also detected the nonlinear Meissner response at edges and defects in superconducting samples (131).

3.5.3. Imaging microwave fields. Near-field microwave probes have been used to map out the gigahertz fields in microwave resonators (132) and metamaterials (133), where the characteristic length scale is determined by the EM wavelength and mesoscopic resolution is not necessary. The spatial mapping of a time-varying *E*-field that accompanies SAWs in piezoelectrics, however, does require a nanoscale probe due to the micrometer-sized gigahertz acoustic wavelength. The configuration is different from the imaging of transduction loss (Section 3.4) in that the tip is acting as a receiver to detect the microwave fields launched from a nearby transducer. Such acoustic field imaging has been recently demonstrated on SAW components (134) and resonators (135), which may find applications in electroacoustic devices, quantum acoustics, and phononic crystals.

4. SUMMARY AND OUTLOOK

In summary, the past decade has witnessed the upturn of near-field microwave microscopy, especially in the form of MIM, in various branches of materials research. By quantitatively imaging on the nanoscale, the dielectric constant and conductivity can be obtained on novel semiconductors, photoconductors, and biological materials. Implementation of the technique in cryogenic and magnetic-field environments has led to important discoveries in materials with strong correlation and topological order. The understanding of MIM contrast in ferroelectric DWs and piezoelectrics also expands its territory into dipolar materials and electromechanical systems.

Having surveyed the major progress of MIM in recent years, we conclude that the technique has arrived at a critical juncture for future prosperity. The success of a particular SPM mode depends on multiple conditions: (*a*) commercial companies supplying the specialized probes, electronics, and platforms compatible with the module; (*b*) a broad user community, ideally including both

industrial teams and academic groups; and (*c*) widespread applications, ideally including general-purpose imaging and killer applications in frontier research. As detailed in this review, the rapid progress of MIM in the past decade has addressed these key points with positive answers, which certainly bodes well for the future.

It is also interesting to ponder the ultimate limits of microwave microscopy in the next few decades. A number of desired functionalities and applications are discussed below.

4.1. Spatial Resolution

Except for the configurations based on tunneling (136) and nonlinearity (137), the spatial resolution of NSMM with linear dielectric contrast has been limited to ∼50 nm for most reports to date. Further improvement would require a concerted effort to construct durable and sharp tips, sensitive electronics, and reliable feedback control from the scanner. We anticipate that sub-10-nm resolution can be achieved within the next decade.

4.2. Operation Frequency

Beyond the current MIM frequency band (from low MHz to ∼20 GHz), the probe and electronics become progressively harder to construct. On the other hand, material properties in the millimeter-wave (30–300 GHz) regime are of great interest for civil and military applications. Microscopy around 10^{11} Hz will also bridge the gap between the current frequencies of NSMM (up to $\sim 10^{10}$ Hz) and NSOM (down to $\sim 10^{12}$ Hz). With efforts along this direction (138–140), near-field imaging throughout the EM spectrum may happen in one or two decades.

4.3. Industrial Applications

As discussed above, microwave microscopy could be appealing for multi-billion-dollar industries such as semiconductor technology, photovoltaics, and SAW devices. Industrial applications usually require high-throughput, large-scale (e.g., wafer-scale) inspection and fast (e.g., video-speed) operation, which necessitate building suitable probes, electronics, and scanning platforms. The ability to zoom out for coarse imaging and zoom in for fine scanning would be desirable as well. It is hopeful that MIM will become the standard tool for multiple industries in the future.

4.4. Academic Applications

The broad range of MIM applications reviewed here is a good start for cutting-edge scientific studies. For complex systems with various degrees of freedom, it is usually advantageous to perform multimodality microscopy. One may further envision the integration of MIM with NSOM, electrostatic force microscopy, Kelvin probe force microscopy, and magnetic force microscopy, among others, in one experiment. In addition, the research of quantum materials may require extreme conditions, such as milli-Kelvin temperature in a dilution refrigerator (141) or ultrahigh vacuum in a molecular-beam epitaxy chamber. Efforts are underway to incorporate MIM into these instruments, which will continue to bring us exciting discoveries in materials research.

DISCLOSURE STATEMENT

K.L. holds a patent on MIM technology, which is licensed to PrimeNano Inc. for commercial instruments. The terms of this arrangement have been reviewed and approved by the University of

Texas at Austin in accordance with its policy on objectivity in research. The remaining authors are not aware of any affiliations, memberships, funding, or financial holdings that might be perceived as affecting the objectivity of this review.

ACKNOWLEDGMENTS

K.L. is supported by the US Department of Energy, Office of Science, Basic Energy Sciences, under award DE-SC0019025 for the preparation of this manuscript. Z.C. acknowledges support from Welch Foundation grant F-1814. L.Z. is supported by National Science Foundation award DMR-1707372.

LITERATURE CITED

1. Jackson JD. 1999. *Classical Electrodynamics*. New York: Wiley. 3rd ed.
2. Betzig E, Trautman JK. 1992. Near-field optics: microscopy, spectroscopy, and surface modification beyond the diffraction limit. *Science* 257:189–95
3. Dunn RC. 1999. Near-field scanning optical microscopy. *Chem. Rev.* 99:2891–928
4. Rosner BT, van der Weide DW. 2002. High-frequency near-field microscopy. *Rev. Sci. Instrum.* 73:2505–25
5. Xiang XD, Gao C. 2002. Quantitative complex electrical impedance microscopy by scanning evanescent microwave microscope. *Mater. Charact.* 48:117–25
6. Anlage SM, Talanov VV, Schwartz AR. 2006. Principles of near-field microwave microscopy. In *Scanning Probe Microscopy: Electrical and Electromechanical Phenomena at the Nanoscale*, ed. SV Kalinin, A Gruverman, pp. 215–53. New York: Springer
7. Lai K, Kundhikanjana W, Kelly MA, Shen ZX. 2011. Nanoscale microwave microscopy using shielded cantilever probes. *Appl. Nanosci.* 1:13–18
8. Synge EH. 1928. A suggested method for extending the microscopic resolution into the ultramicroscopic region. *Philos. Mag.* 6:356–62
9. Soohoo RF. 1962. A microwave magnetic microscope. *J. Appl. Phys.* 33:1276–77
10. Bryant CA, Gunn JB. 1965. Noncontact technique for the local measurement of semiconductor resistivity. *Rev. Sci. Instrum.* 36:1614–17
11. Ash EA, Nicholls G. 1972. Super-resolution aperture scanning microscope. *Nature* 237:510–12
12. Fee M, Chu S, Hansch TW. 1989. Scanning electromagnetic transmission line microscope with sub-wavelength resolution. *Opt. Commun.* 69:219–24
13. Binnig G, Rohrer H, Gerber Ch, Weibel E. 1982. Surface studies by scanning tunneling microscopy. *Phys. Rev. Lett.* 49:57–61
14. Binnig G, Quate CF, Gerber Ch. 1986. Atomic force microscope. *Phys. Rev. Lett.* 56:930–33
15. Tabib-Azar M, Shoemaker NS, Harris S. 1993. Non-destructive characterization of materials by evanescent microwaves. *Meas. Sci. Technol.* 4:583–90
16. Golosovsky M, Davidov D. 1996. Novel millimeter-wave near-field resistivity microscope. *Appl. Phys. Lett.* 68:1579–81
17. Wei T, Xiang XD, Wallace-Freedman WG, Schultz PG. 1996. Scanning tip microwave near-field microscope. *Appl. Phys. Lett.* 68:3506–8
18. Vlahacos CP, Black RC, Anlage SM, Amar A, Wellstood FC. 1996. Near-field scanning microwave microscope with 100 μm resolution. *Appl. Phys. Lett.* 69:3272–74
19. van der Weide DW. 1997. Localized picosecond resolution with a near-field microwave/scanning-force microscope. *Appl. Phys. Lett.* 70:677–79
20. Gao C, Wei T, Duewer F, Lu Y, Xiang XD. 1997. High spatial resolution quantitative microwave impedance microscopy by a scanning tip microwave near-field microscope. *Appl. Phys. Lett.* 71:1872–74
21. Tabib-Azar M, Wang Y. 2004. Design and fabrication of scanning near-field microwave probes compatible with atomic force microscopy to image embedded nanostructures. *IEEE Trans. Microw. Theory Tech.* 52:971–79

22. Wang Y, Bettermann AD, van der Weide DW. 2007. Process for scanning near-field microwave microscope probes with integrated ultratall coaxial tips. *J. Vac. Sci. Technol. B* 25:813–16
23. Lai K, Ji MB, Leindecker N, Kelly MA, Shen ZX. 2007. Atomic force-microscope-compatible near-field scanning microwave microscope with separated excitation and sensing probes. *Rev. Sci. Instrum.* 78:063702
24. Karbassi A, Ruf D, Bettermann AD, Paulson CA, van der Weide DW, et al. 2008. Quantitative scanning near-field microwave microscopy for thin film dielectric constant measurement. *Rev. Sci. Instrum.* 79:094706
25. Huber HP, Moertelmaier M, Wallis TM, Chiang CJ, Hochleitner M, et al. 2010. Calibrated nanoscale capacitance measurements using a scanning microwave microscope. *Rev. Sci. Instrum.* 81:113701
26. Zhang L, Ju Y, Hosoi A, Fujimoto A. 2010. Microwave atomic force microscopy imaging for nanometer-scale electrical property characterization. *Rev. Sci. Instrum.* 81:123708
27. Kundhikanjana W, Lai K, Kelly MA, Shen ZX. 2011. Cryogenic microwave imaging of metal–insulator transition in doped silicon. *Rev. Sci. Instrum.* 82:033705
28. Lai K, Kundhikanjana W, Kelly MA, Shen ZX. 2008. Modeling and characterization of a cantilever-based near-field scanning microwave impedance microscope. *Rev. Sci. Instrum.* 79:063703
29. Yang Y, Lai K, Tang Q, Kundhikanjana W, Kelly MA, et al. 2012. Batch-fabricated cantilever probes with electrical shielding for nanoscale dielectric and conductivity imaging. *J. Micromech. Microeng.* 22:115040
30. Cui YT, Ma EY, Shen ZX. 2016. Quartz tuning fork based microwave impedance microscopy. *Rev. Sci. Instrum.* 87:063711
31. Wu X, Hao Z, Wu D, Zheng L, Jiang Z, et al. 2018. Quantitative measurements of nanoscale permittivity and conductivity using tuning fork-based microwave impedance microscopy. *Rev. Sci. Instrum.* 89:043704
32. Cui YT, Ma EY. 2018. Microwave impedance microscopy. In *Capacitance Spectroscopy of Semiconductors*, ed. JV Li, G Ferrari, pp. 411–35. Boca Raton, FL: CRC Press
33. Kundhikanjana W, Yang Y, Tanga Q, Zhang K, Lai K, et al. 2013. Unexpected surface implanted layer in static random access memory devices observed by microwave impedance microscope. *Semicond. Sci. Technol.* 28:025010
34. Gao C, Xiang XD. 1998. Quantitative microwave near-field microscopy of dielectric properties. *Rev. Sci. Instrum.* 69:3846–51
35. Gao C, Duewer F, Xiang XD. 1999. Quantitative microwave evanescent microscopy. *Appl. Phys. Lett.* 75:3005–7
36. Steinhauer DE, Vlahacos CP, Wellstood FC, Anlage SM, Canedy C, et al. 2000. Quantitative imaging of dielectric permittivity and tunability with a near-field scanning microwave microscope. *Rev. Sci. Instrum.* 71:2751–58
37. Gao C, Hu B, Zhang P, Huang M, Liu W, et al. 2004. Quantitative microwave evanescent microscopy of dielectric thin films using a recursive image charge approach. *Appl. Phys. Lett.* 84:4647–49
38. Wu D, Pak AJ, Liu Y, Zhou Y, Wu X, et al. 2015. Thickness-dependent dielectric constant of few-layer In_2Se_3 nanoflakes. *Nano Lett.* 15:8136–40
39. Han G, Chen ZG, Drennan J, Zou J. 2014. Indium selenides: structural characteristics, synthesis and their thermoelectric performances. *Small* 10:2747–65
40. Kumar A, Ahluwalia PK. 2012. Tunable dielectric response of transition metals dichalcogenides MX_2 (M = Mo, W; X = S, Se,Te): effect of quantum confinement. *Physica B* 407:4627–34
41. Vander Vorst A, Rosen A, Kotsuka Y. 2006. *RF/Microwave Interaction with Biological Tissues*. Hoboken, NJ: Wiley
42. Biagi MC, Fabregas R, Gramse G, van der Hofstadt M, Juárez A, et al. 2016. Nanoscale electric permittivity of single bacterial cells at gigahertz frequencies by scanning microwave microscopy. *ACS Nano* 10:280–88
43. Wang Z, Kelly MA, Shen ZX, Wang G, Xiang XD, et al. 2002. Evanescent microwave probe measurement of low-k dielectric films. *J. Appl. Phys.* 92:808–11
44. Lai K, Kundhikanjana W, Kelly MA, Shen ZX. 2008. Calibration of shielded microwave probes using bulk dielectrics. *Appl. Phys. Lett.* 93:123105
45. Ruess FJ, Oberbeck L, Simmons MY, Goh KEJ, Hamilton AR. 2014. Toward atomic-scale device fabrication in silicon using scanning probe microscopy. *Nano Lett.* 10:1969–73

46. Gramse G, Kölker A, Lim T, Stock TJZ, Solanki H, et al. 2017. Nondestructive imaging of atomically thin nanostructures buried in silicon. *Sci. Adv.* 3:e1602586
47. Tselev A, Velmurugan J, Ievlev AV, Kalinin SV, Kolmakov A. 2016. Seeing through walls at the nanoscale: microwave microscopy of enclosed objects and processes in liquids. *ACS Nano* 10:3562–70
48. Torigoe K, Arita M, Motooka T. 2012. Sensitivity analysis of scanning microwave microscopy for nanoscale dopant measurements in Si. *J. Appl. Phys.* 111:104325
49. Brinciotti E, Gramse G, Hommel S, Schweinboeck T, Altes A, et al. 2015. Probing resistivity and doping concentration of semiconductors at the nanoscale using scanning microwave microscopy. *Nanoscale* 7:14715–22
50. Buchter A, Hoffmann J, Delvallée A, Brinciotti E, Hapiuk D, et al. 2018. Scanning microwave microscopy applied to semiconducting GaAs structures. *Rev. Sci. Instrum.* 89:023704
51. Wang WH, Kalantar-Zadeh K, Kis A, Coleman JN, Strano MS. 2012. Electronics and optoelectronics of two-dimensional transition metal dichalcogenides. *Nat. Nanotechnol.* 7:699–712
52. Wu D, Li X, Luan L, Wu X, Li W, et al. 2016. Uncovering edge states and electrical inhomogeneity in MoS_2 field-effect transistors. *PNAS* 113:8583–88
53. Lai K, Peng H, Kundhikanjana W, Schoen DT, Xie C, et al. 2009. Nanoscale electronic inhomogeneity in In_2Se_3 nanoribbons revealed by microwave impedance microscopy. *Nano Lett.* 9:1265–69
54. Kundhikanjana W, Lai K, Wang H, Dai H, Kelly MA, et al. 2009. Hierarchy of electronic properties of chemically derived and pristine graphene probed by microwave imaging. *Nano Lett.* 9:3762–65
55. Liu Y, Ghosh R, Wu D, Ismach A, Ruoff R, et al. 2014. Mesoscale imperfections in MoS_2 atomic layers grown by a vapor transport technique. *Nano Lett.* 14:4682–86
56. Berweger S, Weber JC, John J, Velazquez JM, Pieterick A, et al. 2015. Microwave near-field imaging of two-dimensional semiconductors. *Nano Lett.* 15:1122–27
57. Liu Y, Tan C, Chou H, Nayak A, Wu D, et al. 2015. Thermal oxidation of WSe_2 nanosheets adhered on SiO_2/Si substrates. *Nano Lett.* 15:4979–84
58. Kim JS, Liu Y, Zhu W, Kim S, Wu D, et al. 2015. Toward air-stable multilayer phosphorene thin-films and transistors. *Sci. Rep.* 5:8989
59. Tan C, Liu Y, Chou H, Kim JS, Wu D, et al. 2016. Laser-assisted oxidation of multi-layer tungsten diselenide nanosheets. *Appl. Phys. Lett.* 108:083112
60. de Visser PJ, Chua R, Island JO, Finkel M, Katan AJ, et al. 2016. Spatial conductivity mapping of unprotected and capped black phosphorus using microwave microscopy. *2D Mater.* 3:021002
61. Berweger S, Qiu G, Wang Y, Pollard B, Genter KL, et al. 2019. Imaging carrier inhomogeneities in ambipolar tellurene field effect transistors. *Nano Lett.* 19:1289–94
62. Wu D, Li W, Rai A, Wu X, Movva HCP, et al. 2019. Visualization of local conductance in MoS_2/WSe_2 heterostructure transistors. *Nano Lett.* 19:1976–81
63. Seabron E, MacLaren S, Xie X, Rotkin SV, Rogers JA, et al. 2016. Scanning probe microwave reflectivity of aligned single-walled carbon nanotubes: imaging of electronic structure and quantum behavior at the nanoscale. *ACS Nano* 10:360–68
64. Matey JR, Blanc J. 1985. Scanning capacitance microscopy. *J. Appl. Phys.* 57:1437–44
65. Imtiaz A, Wallis TM, Weber JC, Coakley KJ, Brubaker MD, et al. 2014. Imaging the p-n junction in a gallium nitride nanowire with a scanning microwave microscope. *Appl. Phys. Lett.* 104:263107
66. Berweger S, Blanchard PT, Brubaker MD, Coakley KJ, Sanford NA, et al. 2016. Near-field control and imaging of free charge carrier variations in GaN nanowires. *Appl. Phys. Lett.* 108:073101
67. Choi W, Seabron E, Mohseni PK, Kim JD, Gokus T, et al. 2017. Direct electrical probing of periodic modulation of zinc-dopant distributions in planar gallium arsenide nanowires. *ACS Nano* 11:1530–39
68. Miller SL, McWhorter PJ. 1992. Physics of the ferroelectric nonvolatile memory field effect transistor. *J. Appl. Phys.* 72:5999–6010
69. Fujimoto T, Awaga K. 2013. Electric-double-layer field-effect transistors with ionic liquids. *Phys. Chem. Chem. Phys.* 15:8983–9006
70. Ponath P, Fredrickson K, Posadas AB, Ren Y, Wu X, et al. 2015. Carrier density modulation in a germanium heterostructure by ferroelectric switching. *Nat. Commun.* 6:6067

71. Ren Y, Yuan H, Wu X, Chen Z, Iwasa Y, et al. 2015. Direct imaging of nanoscale conductance evolution in ion-gel-gated oxide transistors. *Nano Lett*. 15:4730–36
72. Gu Y, Kwak ES, Lensch JL, Allen JE, Odom TW, et al. 2005. Near-field scanning photocurrent microscopy of a nanowire photodetector. *Appl. Phys. Lett.* 87:043111
73. Brenner TM, Egger DA, Kronik L, Hodes G, Cahen D. 2016. Hybrid organic-inorganic perovskites: low-cost semiconductors with intriguing charge-transport properties. *Nat. Rev. Mater.* 1:15007
74. Chu Z, Yang M, Schulz P, Wu D, Ma X, et al. 2017. Impact of grain boundaries on efficiency and stability of organic-inorganic trihalide perovskites. *Nat. Commun.* 8:2230
75. Geim AK, Grigorieva IV. 2013. Van der Waals heterostructures. *Nature* 499:419–25
76. Novoselov KS, Mishchenko A, Carvalho A, Castro Neto AH. 2016. 2D materials and van der Waals heterostructures. *Science* 353:aac9439
77. Chu Z, Han A, Lei C, Lopatin S, Li P, et al. 2018. Energy-resolved photoconductivity mapping in a monolayer-bilayer WSe_2 lateral heterostructure. *Nano Lett*. 18:7200–6
78. Tsai Y, Chu Z, Han Y, Chuu CP, Wu D, et al. 2017. Tailoring semiconductor lateral multijunctions for giant photoconductivity enhancement. *Adv. Mater.* 29:1703680
79. Berweger S, MacDonald GA, Yang M, Coakley KJ, Berry JJ, et al. 2017. Electronic and morphological inhomogeneities in pristine and deteriorated perovskite photovoltaic films. *Nano Lett*. 17:1796–801
80. Johnston SR, Ma EY, Shen ZX. 2018. Optically coupled methods for microwave impedance microscopy. *Rev. Sci. Instrum.* 89:043703
81. Dagotto E. 2005. Complexity in strongly correlated electronic systems. *Science* 309:257–62
82. Imada M, Fujimori A, Tokura Y. 1998. Metal-insulator transitions. *Rev. Mod. Phys.* 70:1039–263
83. Lai K, Nakamura M, Kundhikanjana W, Kawasaki M, Tokura Y, et al. 2010. Mesoscopic percolating resistance network in a strained manganite thin film. *Science* 329:190–93
84. Tselev A, Strelcov E, Luk'yanchuk IA, Budai JD, Tischler JZ, et al. 2010. Interplay between ferroelastic and metal-insulator phase transitions in strained quasi-two-dimensional VO_2 nanoplatelets. *Nano Lett*. 10:2003–11
85. Tselev A, Lavrik NV, Kolmakov A, Kalinin SV. 2013. Scanning near-field microwave microscopy of VO_2 and chemical vapor deposition graphene. *Adv. Funct. Mater.* 23:2635–45
86. Kundhikanjana W, Sheng Z, Yang Y, Lai K, Ma EY, et al. 2015. Direct imaging of dynamic glassy behavior in a strained manganite film. *Phys. Rev. Lett.* 115:265701
87. Schulz HJ. 1990. Incommensurate antiferromagnetism in the two-dimensional Hubbard model. *Phys. Rev. Lett.* 64:1445–48
88. Ueda K, Fujioka J, Takahashi Y, Suzuki T, Ishiwata S, et al. 2014. Anomalous domain-wall conductance in pyrochlore-type $Nd_2Ir_2O_7$ on the verge of the metal-insulator transition. *Phys. Rev. B* 89:075127
89. Ma EY, Cui YT, Ueda K, Tang S, Chen K, et al. 2015. Mobile metallic domain walls in an all-in-all-out magnetic insulator. *Science* 350:538–41
90. Ma EY, Bryant B, Tokunaga Y, Aeppli G, Tokura Y, et al. 2015. Charge-order domain walls with enhanced conductivity in a layered manganite. *Nat. Commun.* 6:7595
91. Fischer O, Kugler M, Maggio-Aprile I, Berthod C, Renner C. 2007. Scanning tunneling spectroscopy of high-temperature superconductors. *Rev. Mod. Phys.* 79:353–419
92. Liu M, Sternbach AJ, Basov DN. 2016. Nanoscale electrodynamics of strongly correlated quantum materials. *Rep. Prog. Phys.* 80:014501
93. Wen XG. 1990. Topological orders in rigid states. *Int. J. Mod. Phys. B* 4:239–71
94. Chang CZ, Li M. 2016. Quantum anomalous Hall effect in time-reversal-symmetry breaking topological insulators. *J. Phys. Condens. Matter* 28:123002
95. von Klitzing K, Dorda G, Pepper M. 1980. New method for high-accuracy determination of the fine-structure constant based on quantized Hall resistance. *Phys. Rev. Lett.* 45:494–97
96. Lai K, Kundhikanjana W, Kelly MA, Shen ZX, Shabani J, et al. 2011. Imaging of Coulomb-driven quantum Hall edge states. *Phys. Rev. Lett.* 107:176809
97. Chklovskii DB, Shklovskii BI, Glazman LI. 1992. Electrostatics of edge channels. *Phys. Rev. B* 46:4026–34

98. Cui YT, Wen B, Ma EY, Diankov G, Han Z, et al. 2016. Unconventional correlation between quantum Hall transport quantization and bulk state filling in gated graphene devices. *Phys. Rev. Lett.* 117:186601
99. Kane CL, Mele EJ. 2005. Z_2 topological order and the quantum spin Hall effect. *Phys. Rev. Lett.* 95:146802
100. Bernevig BA, Zhang SC. 2006. Quantum spin Hall effect. *Phys. Rev. Lett.* 96:106802
101. Ma EY, Calvo MR, Wang J, Lian B, Muhlbauer M, et al. 2015. Unexpected edge conduction in mercury telluride quantum wells under broken time-reversal symmetry. *Nat. Commun.* 6:7252
102. Bernevig BA, Hughes TL, Zhang SC. 2006. Quantum spin Hall effect and topological phase transition in HgTe quantum wells. *Science* 314:1757–61
103. König M, Wiedmann S, Brüne C, Roth A, Buhmann H, et al. 2007. Quantum spin Hall insulator state in HgTe quantum wells. *Science* 318:766–70
104. Shi Y, Kahn J, Niu B, Fei Z, Sun B, et al. 2019. Imaging quantum spin Hall edges in monolayer WTe_2. *Sci. Adv.* 5:eaat8799
105. Yu R, Zhang W, Zhang HJ, Zhang SC, Dai X, et al. 2010. Quantized anomalous Hall effect in magnetic topological insulators. *Science* 329:61–64
106. Chang CZ, Zhang J, Feng X, Shen J, Zhang Z, et al. 2013. Experimental observation of the quantum anomalous Hall effect in a magnetic topological insulator. *Science* 340:167–70
107. Allen M, Cui Y, Ma EY, Mogi M, Kawamurae M, et al. 2019. Visualization of an axion insulating state at the transition between 2 chiral quantum anomalous Hall states. *PNAS* 116:14511–15
108. Mogi M, Kawamura M, Yoshimi R, Tsukazaki A, Kozuka Y, et al. 2017. A magnetic heterostructure of topological insulators as a candidate for an axion insulator. *Nat. Mater.* 16:516–21
109. Grauer S, Fijalkowski KM, Schreyeck S, Winnerlein M, Brunner K, et al. 2017. Scaling of the quantum anomalous Hall effect as an indicator of axion electrodynamics. *Phys. Rev. Lett.* 118:246801
110. Xiao D, Jiang J, Shin JH, Wang W, Wang F, et al. 2018. Realization of the axion insulator state in quantum anomalous Hall sandwich heterostructures. *Phys. Rev. Lett.* 120:056801
111. Jonscher AK. 1999. Dielectric relaxation in solids. *J. Phys. D* 32:R57–70
112. Kittel C. 1951. Domain boundary motion in ferroelectric crystals and the dielectric constant at high frequency. *Phys. Rev.* 83:458
113. Maglione M, Böhmer R, Loidl A, Höchli UT. 1989. Polar relaxation mode in pure and iron doped barium titanate. *Phys. Rev. B* 40:11441–44
114. Arlt G, Böttger U, Witte S. 1994. Dielectric dispersion of ferroelectric ceramics and single crystals at microwave frequencies. *Ann. Phys.* 3:578–88
115. Seidel J, Martin LW, He Q, Zhan Q, Chu YH, et al. 2009. Conduction at domain walls in oxide multiferroics. *Nat. Mater.* 8:229–34
116. Vasudevan RK, Wu W, Guest JR, Baddorf AP, Morozovska AN, et al. 2013. Domain wall conduction and polarization-mediated transport in ferroelectrics. *Adv. Funct. Mater.* 23:2592–616
117. Lummen TTA, Leung J, Kumar A, Wu X, Ren Y, et al. 2017. Emergent low-symmetry phases and large property enhancements in ferroelectric $KNbO_3$ bulk crystals. *Adv. Mater.* 29:1700530
118. Tselev A, Yu P, Cao Y, Dedon LR, Martin LW, et al. 2016. Microwave a.c. conductivity of domain walls in ferroelectric thin films. *Nat. Commun.* 7:11630
119. Wu X, Petralanda U, Zheng L, Ren Y, Hu R, et al. 2017. Low-energy structural dynamics of ferroelectric domain walls in hexagonal rare-earth manganites. *Sci. Adv.* 3:e1602371
120. Choi T, Horibe Y, Yi HT, Choi YJ, Wu W, et al. 2010. Insulating interlocked ferroelectric and structural antiphase domain walls in multiferroic $YMnO_3$. *Nat. Mater.* 9:253–58
121. Wu X, Du K, Zheng L, Wu D, Cheong SW, et al. 2018. Microwave conductivity of ferroelectric domains and domain walls in a hexagonal rare-earth ferrite. *Phys. Rev. B* 98:081409(R)
122. Grüner G. 1988. The dynamics of charge-density waves. *Rev. Mod. Phys.* 60:1129–81
123. Chen Y, Lewis RM, Engel LW, Tsui DC, Ye PD, et al. 2003. Microwave resonance of the 2D Wigner crystal around integer Landau fillings. *Phys. Rev. Lett.* 91:016801
124. Weigel R, Morgan DP, Owens JM, Ballato A, Lakin KM, et al. 2002. Microwave acoustic materials, devices, and applications. *IEEE Trans. Microw. Theory Tech.* 50:738–49

125. Johnston SR, Yang Y, Cui YT, Ma EY, Kämpfe T, et al. 2017. Measurement of surface acoustic wave resonances in ferroelectric domains by microwave microscopy. *J. Appl. Phys.* 122:074101
126. Zheng L, Dong H, Wu X, Huang YL, Wang W, et al. 2018. Interferometric imaging of nonlocal electromechanical power transduction in ferroelectric domains. *PNAS* 115:5338–42
127. Royer D, Dieulesaint E. 1999. *Elastic Waves in Solids*. New York: Springer
128. Joseph CH, Sardi GM, Tuca SS, Gramse G, Lucibello A, et al. 2016. Scanning microwave microscopy technique for nanoscale characterization of magnetic materials. *J. Magn. Magn. Mater.* 420:62–69
129. Cho Y, Kirihara A, Saeki T. 1996. Scanning nonlinear dielectric microscope. *Rev. Sci. Instrum.* 67:2297–303
130. Hirose K, Tanahashi K, Takato H, Cho Y. 2017. Quantitative measurement of active dopant density distribution in phosphorusimplanted monocrystalline silicon solar cell using scanning nonlinear dielectric microscopy. *Appl. Phys. Lett.* 111:032101
131. Lee SC, Anlage SM. 2003. Study of local nonlinear properties using a near-field microwave microscope. *IEEE Trans. Appl. Supercond.* 13:3594–97
132. Dutta SK, Vlahacos CP, Steinhauer DE, Thanawalla AS, Feenstra BJ, et al. 1999. Imaging microwave electric fields using a near-field scanning microwave microscope. *Appl. Phys. Lett.* 74:156–58
133. Gao F, Xue H, Yang Z, Lai K, Yu Y, et al. 2018. Topologically protected refraction of robust kink states in valley photonic crystals. *Nat. Phys.* 14:140–44
134. Zheng L, Wu D, Wu X, Lai K. 2018. Visualization of surface-acoustic-wave potential by transmission-mode microwave impedance microscopy. *Phys. Rev. Appl.* 9:061002
135. Shao L, Maity S, Zheng L, Wu L, Shams-Ansari A, et al. 2019. Phononic band structure engineering for high-Q gigahertz surface acoustic wave resonators on lithium niobate. *Phys. Rev. Appl.* 12:014022
136. Lee J, Long CJ, Yang H, Xiang XD, Takeuchi I. 2010. Atomic resolution imaging at 2.5 GHz using near-field microwave microscopy. *Appl. Phys. Lett.* 97:183111
137. Cho Y, Hirose R. 2007. Atomic dipole moment distribution of Si atoms on a Si(111)-(7×7) surface studied using noncontact scanning nonlinear dielectric microscopy. *Phys. Rev. Lett.* 99:186101
138. Park W, Kim J, Lee K. 2001. Millimeter-wave scanning near-field microscope using a resonant waveguide probe. *Appl. Phys. Lett.* 79:2642–44
139. Kim M, Kim J, Kim H, Kim S, Yang J, et al. 2004. Nondestructive high spatial resolution imaging with a 60 GHz near-field scanning millimeter-wave microscope. *Rev. Sci. Instrum.* 75:684–88
140. Finkel M, Thierschmann H, Katan AJ, Westig MP, Spirito M, et al. 2019. Shielded cantilever with on-chip interferometer circuit for THz scanning probe impedance microscopy. *Rev. Sci. Instrum.* 90:113701
141. Geaney S, Cox D, Hönigl-Decrinis T, Shaikhaidarov R, Kubatkin SE, et al. 2019. Near-field scanning microwave microscopy in the single photon regime. arXiv:1902.08066 [physics.app-ph]